Lab on a Chip

PAPER

View Article Online
View Journal | View Issue

Cite this: *Lab Chip*, 2025, **25**, 440

Injury-on-a-chip for modelling microvascular trauma-induced coagulation†

Halston Deal,[ab] Elizabeth M. Byrnes,[a] Sanika Pandit,[ab] Anastasia Sheridan,[ab] Ashley C. Brown *[ab] and Michael Daniele *[abc]

Received 31st May 2024,
Accepted 5th December 2024

DOI: 10.1039/d4lc00471j

rsc.li/loc

Blood coagulation is a highly regulated injury response that features polymerization of fibrin fibers to prevent the passage of blood from a damaged vascular endothelium. A growing body of research seeks to monitor coagulation in microfluidic systems but fails to capture coagulation as a response to disruption of the vascular endothelium. Here we present a device that allows compression injury of a defined segment of a microfluidic vascular endothelium and the assessment of coagulation at the injury site. This pressure injury-on-a-chip (PINCH) device allows visualization of coagulation as the accumulation of fluorescent fibrin at injury sites. Quantification of fluorescent fibrin levels upstream of and at injury sites confirm that pre-treating vascular endothelium with fluid shear stress helps capture coagulation as an injury response. We leverage the PINCH devices to demonstrate the limited coagulation response of type A hemophiliacs and evaluate the performance of hemostatic microparticles and fibrinolytic nanoparticles. Our findings and the straightforward fabrication of the PINCH devices make it a promising choice for additional screening of hemostatic therapeutics.

1. Introduction

Upon injury, damaged vascular and adventitial cells release and expose procoagulant factors that initiate hemostasis. Hemostasis features the attachment of platelets to exposed extracellular matrix (ECM) and the entanglement of platelets with fibrin to stop bleeding. The polymerization of fibrinogen monomers into fibrin is known as coagulation. The hemostatic transition to phase separation of fibrin is highly regulated, but is aberrant in numerous pathologies including hemophilia, disseminated intravascular coagulation (DIC), diabetes, stroke, and von Willebrand's Disease, to name a few.[1–4] Numerous models exist for studying characteristics of and treatments for dysregulated coagulation. However, few models capture human-specific coagulation as a response to damage to vascular tissue. The growth of microphysiological systems (MPS) engineering has led to an increased consideration of microfluidic technology for monitoring coagulation.[5–10]

Dozens of microfluidic devices have been engineered to study hemostasis.[6,7,9–12] Researchers have promoted coagulation with microchannel features like collagen and tissue factor (TF) coating,[13–17] stenoses,[17–26] and fluid shear dead zones.[27,28] However, few devices have enabled coagulation as a response to damage of a vascular endothelium.[29–32] Chen *et al.* damaged blood vessel endothelial cells in a microchannel with ultraviolet irradiation and demonstrated increased coagulation rates with microplastic contamination.[31] Mechanical stimulus has been used to induce vascular endothelial injury with a pneumatic valve and an acupuncture needle.[29,30] Sakurai *et al.* engineered a poly(dimethyl siloxane) (PDMS) valve to allow passage of blood into an open wound microchannel, and Poventud-Fuentes *et al.* leveraged needle puncture to connect a vascular microchannel to a wound microchannel through a punctured collagen gel. While both devices provide a high level of physiological relevance by simulating the passage of whole blood from a primary vessel into wound space, the devices require multi-layer PDMS assembly and neither work evaluates the tendency of coagulation to occur off-site from injury.

There are a variety of fabrication methods for *in vitro* microvascular models. One popular approach is addition of a homogenous suspension of cells and hydrogel into a microchannel. Given various combinations of time, stromal cells, and growth factors within various hydrogels, blood vessel endothelial cells will assemble into perfusable

[a] *Joint Department of Biomedical Engineering, North Carolina State University and University of North Carolina, Chapel Hill, 1840 Entrepreneur Dr., Raleigh, NC, 27695 USA. E-mail: mdaniel6@ncsu.edu*
[b] *Comparative Medicine Institute, North Carolina State University, 1060 William Moore Dr., Raleigh, NC 27606, USA. E-mail: aecarso2@ncsu.edu*
[c] *Department of Electrical & Computer Engineering, North Carolina State University, 890 Oval Dr., Raleigh, NC, 27695 USA*

† Electronic supplementary information (ESI) available. See DOI: https://doi.org/10.1039/d4lc00471j

networks[33–36] or organoids.[37] Other unique fabrication approaches include layering collagen and cells around a Dacron mesh;[38] perfusion of hollow, extruded hydrogel fibers with microvascular cells and embedding the fibers within a hydrogel network;[39–41] soft lithography casting gelatin microchannels;[42] perfusion of endothelial cells in clotting blood within a microfluidic lattice;[43] culture of endothelial cells on self-rolling substrates;[44] integration of microchannel attachments into 96-well plates;[45,46] and viscous finger patterning of microfluidic molds *via* Hele-Shaw cell plate separation.[47] The simplest and most popular approach is to perfuse ECM-treated microchannels with blood vessel endothelial cells to facilitate their attachment to PDMS microchannel walls.[48–51] Thus far, mechanical stimulation including injury has been achieved with multi-layer devices that feature a variation of the multi-layer Quake valve.[5,50,52–58] To simplify fabrication, while still allowing for injury of vascular cells, we adapted an existing microfluidic design, previously used to trap and sort *C. elegans* worms and fluorescent peptides.[59,60] This design allows lateral compression of microchannel segments, which means microchannels can be fabricated from a monolithic cast of PDMS before bonding to glass. Once we confirmed this pressure injury-on-a-chip (PINCH) device allows injury of a blood vessel endothelium, we used the PINCH device to monitor coagulation at vascular injury sites, and we characterized the role that fluid shear and injury play in regulating coagulation levels. PINCH devices successfully capture coagulation tendencies resulting from vascular injury and endothelial stimulation by shear stress. Upon demonstration of coagulation, we used PINCH devices to evaluate coagulation of samples from hemophilic patients and samples augmented with procoagulant and fibrinolytic formulations of colloidal synthetic platelets. Colloidal particles can be tailored to participate in and promote or disrupt the accumulation of fibrin.[61–65] Ultra deformable polymer cores functionalized with fibrin-binding motifs permit mimicry of platelet binding and fibrin collapse. Loading fibrinolytic agents into core–shell architectures can permit lysis of polymerizing fibrin.[61,65] Some coagulopathies present as requiring procoagulants for treatment, whereas anticoagulants are needed in others, so devices like the PINCH are interesting for the evaluation of particles that alter coagulation generally. Our investigation of coagulation, coagulopathy, and hemostasis-augmenting particles with the PINCH devices demonstrates the validity of a lateral compression actuator for inducing injury in a microfluidic system to monitor coagulation and emphasizes the importance of integrating physiologically relevant mechanical stimuli into MPS.

2. Materials & methods

2.1. PINCH device microchannel fabrication

PINCH devices were prepared by casting PDMS from 3D printed molds. Molds were designed in AutoCAD® (Autodesk) and exported as STL before slicing in CHITUBOX® at 10 μm. Molds with 200 μm × 100 μm (*w x h*) vascular microchannel positives were printed with a Boston Micro Fabrication MicroArch® S240 stereolithographic printer and subsequently coated with 3-(trimethoxysilyl)propyl methacrylate (A174, Sigma) and approximately 3 μm of parylene C (Specialty Coating Systems). To prepare the PDMS microchannels, a layer of 25 : 1 w/w of PDMS base and curing agent was mixed and poured onto the mold. After degassing, the PDMS was baked at 80 °C for 25 min. Following this initial step, degassed 10 : 1 PDMS was poured onto the partially cured 25 : 1 layer. The completed casting was cured for >2 h at 80 °C. After curing, the cast was removed from the mold, cut, and ~1 mm holes were punched into inlets and outlets of the vascular microchannels, and a ~1 mm hole was punched into the actuator microchannels. Glass microscope slides were scrubbed with a polyester swab (Texwipe®) and 2% Hellmanex® III solution. Slides were then sprayed with deionized water and acetone, placed into an acetone bath, and sonicated for at least 15 min. Slides were then rinsed with isopropanol (IPA), dried with pressurized nitrogen gas, and baked on a hotplate set to 110 °C. PDMS was cleaned with Scotch® Magic™ Tape to remove dust and briefly sprayed with acetone and IPA before drying with pressurized nitrogen gas. PDMS was placed microchannel-side-up on a hotplate. PDMS and microscope slides were baked on the hotplate set to 110 °C for at least 5 min. After baking, PDMS and microscope slides were treated with air plasma in a Harrick plasma chamber for 2 min on high power, contact bonded, and placed on a hotplate set to 80 °C for at least 10 min. The hotplate was then allowed to cool to room temperature before removing devices. The bonded PDMS and glass were rested for at least 6 h before pressurizing actuator microchannels. Tubing for actuator and vascular microchannels was prepared as Tygon connected to 90 ° stainless steel syringe tips (Jensen Global), which had been soaked in IPA to allow removal from the plastic fitting on the syringe tips. To prevent passage of air from the actuator microchannels into the vascular microchannels during pressurization, actuator microchannels were filled with a 1 : 1 v/v mix of deionized water and glycerol prior to adding cells to the vascular microchannel. An isolated steel syringe tip was inserted into 5 mm of Tygon® which was then filled with 1 : 1 v/v glycerol and water and inserted into actuator microchannel ports. Air was then displaced by pressurizing actuator microchannels at 200–400 mbar, such that air can escape through the PDMS, and water/glycerol fills the actuator microchannel. Pressure was controlled with an Elveflow Ob1 Mk3 (Elvesys, France) pressure regulator.

2.2. Actuator deformation testing

Actuator deformation was measured as the maximum apparent deformation of an actuator wall upon pressurization. Microchannels were monitored and imaged *via* AmScope™ camera and software on a brightfield

microscope. Pressure was applied with an Elveflow Ob1 Mk3 and an image taken at a particular pressure. Pressures were set by scrolling a computer mouse treadwheel within the Elveflow Smart Interface software pressure controller. Before capturing an image, we allowed the microchannels to deform for at least 5 s. The length of the apparent path between starting point and maximum deformation point was evaluated in ImageJ (NIH).

2.3. Cell culture & vascular microchannel seeding

Human umbilical vein endothelial cells (HUVEC, pooled (n = 3–6), Lonza) were grown with endothelial cell growth medium (EGM2, PromoCell®) in polystyrene cell culture flasks (VWR®). HUVECs are a widely used endothelial cell model due to their ease of isolation, robust growth characteristics, and reproducible expression of key endothelial markers. They provide a popular platform for studying vascular functions such as barrier formation, angiogenesis, and response to shear stress, making them suitable for MPS demonstration.[29–31,58,66,67] While not patient-specific, arterial, or venous endothelium, their generalizability allows for insights into endothelial behavior under controlled conditions. EGM2 was supplemented with gentamicin sulfate (VWR®). Flasks were kept in a humidified incubator at 37 °C and 5% CO_2. Media was changed every 24–72 h. 0.25% w/v Trypsin-EDTA (Gibco™) was used to detach cells for passaging. Cells and flasks were handled in a standard biosafety cabinet during passaging and microfluidic seeding. HUVEC used to seed vascular microchannels were passage 3–7. Vascular microchannels were treated with a plasma corona treater with antenna attachment for 15 s, then rinsed and filled with 70% v/v ethanol in deionized water. Vascular microchannels were then rinsed and filled with 50 μg mL^{-1} fibronectin and incubated for ~2 h. Prior to seeding, HUVEC were incubated with 25 μM CellTracker™ Blue CMAC Dye (ThermoFisher) in Trypsin and EGM2. Microchannels treated with fibronectin were rinsed with EGM2. After dyeing and counting, HUVEC were resuspended at ~30 × 10^6 mL^{-1} in EGM2. The high density helps ensure cells attach to microchannel ceilings. HUVEC were given 15–30 min to attach in an incubator. A syringe was then filled with EGM2 and fitted with a 25 G syringe tip (Jensen Global). The tip was carefully inserted into inlet and outlet ports of vascular microchannels, and the syringe plunger pressed briefly and repeatedly to dislodge and rinse out high-density cell aggregates in the inlets and outlet ports. Tygon tubing with 90° steel tip inserts were filled with EGM2 and attached to inlet and outlet ports. PDMS-glass composites with filled actuator microchannels, cellularized vascular microchannels, and tubing attached constituted fully assembled PINCH devices. After rinsing inlet and outlet ports, vascular microchannels were rinsed at 100 μL min^{-1} for ~1 min to remove unattached cells and incubated for one day. The next day, vascular microchannels were rinsed at 100 μL min^{-1} for ~1 min and either perfused with a peristaltic pump (Ismatec®) or left static during incubation. For shear treatment, 5 dyne cm^{-2} was applied continuously or for 1 h prior to continuous application of 10 dyne cm^{-2}. 5 and 10 dyne cm^{-2} were chosen as common starting points for investigation of the impact of fluid shear on vascular endothelial phenotype.[30,68,69] Specifically, pre-treatment at 5 dyne cm^{-2} has been shown to impact the anticoagulant behavior of a microvascular endothelium by limiting the adhesion of platelets compared to static pre-treatment.[69] The range of fluidic wall shear stresses applied also represent the range commonly experienced in umbilical veins *in vivo* (~0.1–10 dyne cm^{-2}).[70] We connected a 3D printed bubble trap,[71] upstream of each device. Bubble traps were printed on a Profluidics 285D microfluidics printer (CADworks3D) with clear resin, soaked in IPA for 2 min, dried with compressed air, and cured in a UV oven (CADworks3D) for 2 min. Prior to assembly, tubing and bubble traps were soaked in 70% v/v ethanol in deionized water for 20–60 min.

2.4. Microvascular injury & coagulation monitoring

To simulate vascular damage as a stimulus for coagulation, PINCH vascular microchannels were perfused with blood plasma without or after compression injury of a defined site along a HUVEC endothelium. Citrated, platelet-depleted, pooled ($n \geq 50$ donors) human blood plasma was purchased from George King Bio-Medical. A subset of devices that were pre-treated with 5 dyne cm^{-2} of fluid shear stress were perfused with citrated, platelet-depleted plasma from type A hemophiliacs (n = 2 donors). To injure HUVEC, actuator microchannels were pressurized to 1800 mbar for 30 s. Pressure was then returned to 0 mbar. Following injury, vascular microchannels were perfused at 30 μL min^{-1} with 1 : 100 annexin V-TRITC in EGM2 and allowed 10 min incubation at room temperature to dye phosphatidylserine (PSer). Vascular microchannels were then rinsed with EGM2 and perfused with blood plasma at 3 μL min^{-1}. Blood plasma was thawed at 37 °C for at least 20 min and brought to final concentrations of 0.01 M $CaCl_2$ and 50 μg mL^{-1} Alexa-Flour 488 labeled fibrinogen. Perfusion at the injury location was monitored with a Stellaris 5 DMI-8 confocal microscope (Leica) for 30 min with a 10× objective scanning at 1000 Hz. Coagulation movies were created in Leica Application Suite X software as z-stacks cycling through the bottom, center, and top of the microchannel. Coagulation was always monitored at room temperature. After perfusion, a z-stack was generated along the length of the vascular microchannel for analysis of relative coagulation levels along the microchannel at, upstream, and downstream of injury sites. Upstream and downstream were approximately 50 μm away from the edges of the injury site as determined visually by the presence of fluorescently labeled PSer (Fig. S4†). A subset of devices pre-treated at 5 and 10 dyne cm^{-2} were fixed with 4% paraformaldehyde for 20 min before permeabilizing cells with 0.1% Triton X-100 for 10 min, blocking with 2% BSA for 45 min, and immunostaining for von Willebrand factor

(vWF) (bio-techne®, NBP2-34510AF647) at 37 °C for 1 hr. 1X DPBS with calcium and magnesium was used to rinse the vascular microchannels in between each previously described step during staining. All steps were conducted at room temperature unless otherwise stated. DAPI was used to stain nuclei in vascular microchannels prepared at 0, 5, and 10 dyne cm^{-2} fluid shear stress pre-treatment.

2.5. Evaluation of shear response & relative coagulation levels in vascular microchannels

Using Leica Application Suite X, 3-plane maximum intensity projections were created at time points (0, 6, 18, 24, 30 min) from coagulation movies. Fluorescent intensity was calculated in ImageJ. Maximum intensity projections were converted to 8-bit images. The same rectangular region of interest (ROI), ~500 μm wide and 250 μm tall, was centered over each image and the fluorescent intensity measured at each time point. The same brightness and contrast settings were applied to every quantified image. Coagulation site-specificity for injury was evaluated by comparing the relative fluorescent intensity of fibrin upstream and at injury sites. Fluorescent images were split into respective color channels. ROI ~900 μm × 240 μm were drawn as rectangles around the annexin V-TRITC positive injury site and fluorescent intensity measured. ROI were then pasted into the fibrin channel, fluorescence measured, and the process was repeated upstream of the injury. Pearson's correlation coefficient (PCC) was also measured with ImageJ, and the percent change calculated from upstream to injury site for a subset of PINCH devices that received 0 or 5 dyne cm^{-2} shear pre-treatment. A set of PINCH devices pre-treated with 5 and 10 dyne cm^{-2} fluid shear stress were stained for von Willebrand Factor (vWF) after injury and plasma perfusion. vWF fluorescence was measured at and around the injury site similar to fibrin. Nuclear orientation an total vWF expression were evaluated along the center of the microchannels within a 140 × 4000 μm ROI. 140 μm was chosen as lesser than 200 μm to avoid values at the edges of the microchannels from skewing results acquired from maximum projection images. Maximum projections were loaded into ImageJ (FIJI). The 120 × 4000 μm ROI was used to crop the center of the vascular microchannel. Nuclear orientation was evaluated with the Directionality plugin and Fourier Components after binarizing images of nuclei. Total average intensity of vWF was evaluated by measuring the mean fluorescent intensity.

2.6. Coagulation augmentation with hemostatic micro- and nano-gels

A subset of PINCH devices was perfused with plasma mixed with either of two fibrin-targeted micro/nanogel technologies that are hemostatic or fibrinolytic.[61–63] The hemostatic particles, fibrin fragment-E-binding platelet-like particles (Frag-E PLPs) were synthesized as previously described.[63] Briefly, ultralow crosslinked (ULC) poly(*N*-isopropylacrylamide-*co*-acrylic acid) (pNIPAm) microgels were synthesized *via* a precipitation polymerization reaction and fibrin-specific antibodies were covalently coupled to ULC microgels *via* EDC/NHS coupling.

Tissue plasminogen activator-conjugated, fibrin-specific nanogels (tPA-FSNs) are dual-function core–shell nanogels that bind fibrin and release fibrinolytic agent from core–shell interiors. tPA-FSNs were evaluated in the MPS as a control for fibrinolysis. tPA-FSNs were synthesized as previously described.[61] Prior to loading with tPA, FSN core–shell particles were fluorescently labeled.

To fluorescently label particles, Frag-E PLPs and FSNs were separately resuspended at 20 mg ml^{-1} in ultrapure water and mixed with 0.2 M sodium bicarbonate and Alexa Fluor 594 NHS Ester (Succinimidyl Ester, ThermoFisher) at a 1 : 1.5 molar ratio of particle : dye. Following a 1 h incubation, labeled particles were purified using 1000 kDa molecular weight cutoff dialysis tubing (Biotech CE Dialysis Tubing, Spectrum Laboratories) and dialyzed against ultrapure water for 48 h before being lyophilized.

Coagulation data from MPS particle experiments were compared to clot structural data obtained *via* confocal microscopy to allow for comparison with previous studies under static conditions.[63,64,72,73] Briefly, plasma was thawed at 37 °C for at least 20 min and brought to final concentrations of 0.01 M $CaCl_2$ and 50 μg mL^{-1} Alexa-Flour 488 labeled fibrinogen to allow visualization of fibrin fibers. Plasma clots were prepared without particles or with either 1 mg mL^{-1} Frag-E PLPs or tPA-FSNs. Once mixed, 30 μL droplets were trapped between a microscope slide and coverslip adhered by two layers of double-sided Scotch® tape. The glass slide and coverslip were sealed with nail polish hardener to prevent dehydration of the clot. To allow thorough fibrin polymerization, clots were imaged after 2 h. A Stellaris 5 DMI-8 confocal microscope (Leica) was used to generate 5 μm *z*-stacks at 0.36 μm spacing with a 63× water immersion objective and 400 Hz scanning. Maximum intensity projections were generated in Leica Application Suite X software and exported for analysis in ImageJ (NIH). Projections were binarized and the ratio of fibrin fiber pixels to background pixels was calculated to estimate fiber density.

2.7. Data analysis

Data were plotted and analyzed in GraphPad Prism 9. All data is presented as means ± one standard deviation unless otherwise stated. Sample sizes are indicated in the captions of the Figures. Data were assessed with and passed a Shapiro–Wilk normality test ($p > 0.05$) and checked for outliers with the ROUT method (Q = 1%), prior to assessment with statistical comparisons identified in the captions of the Figures. A subset of PINCH devices with vascular microchannels pre-treated at 5 dyne cm^{-2} were used in data presented in Fig. 2–4.

3. Results

3.1. Engineering PINCH: pressure injury-on-a-chip

The PINCH devices (Fig. 1) were engineered to provide compression injury to a vascular microchannel. The PINCH

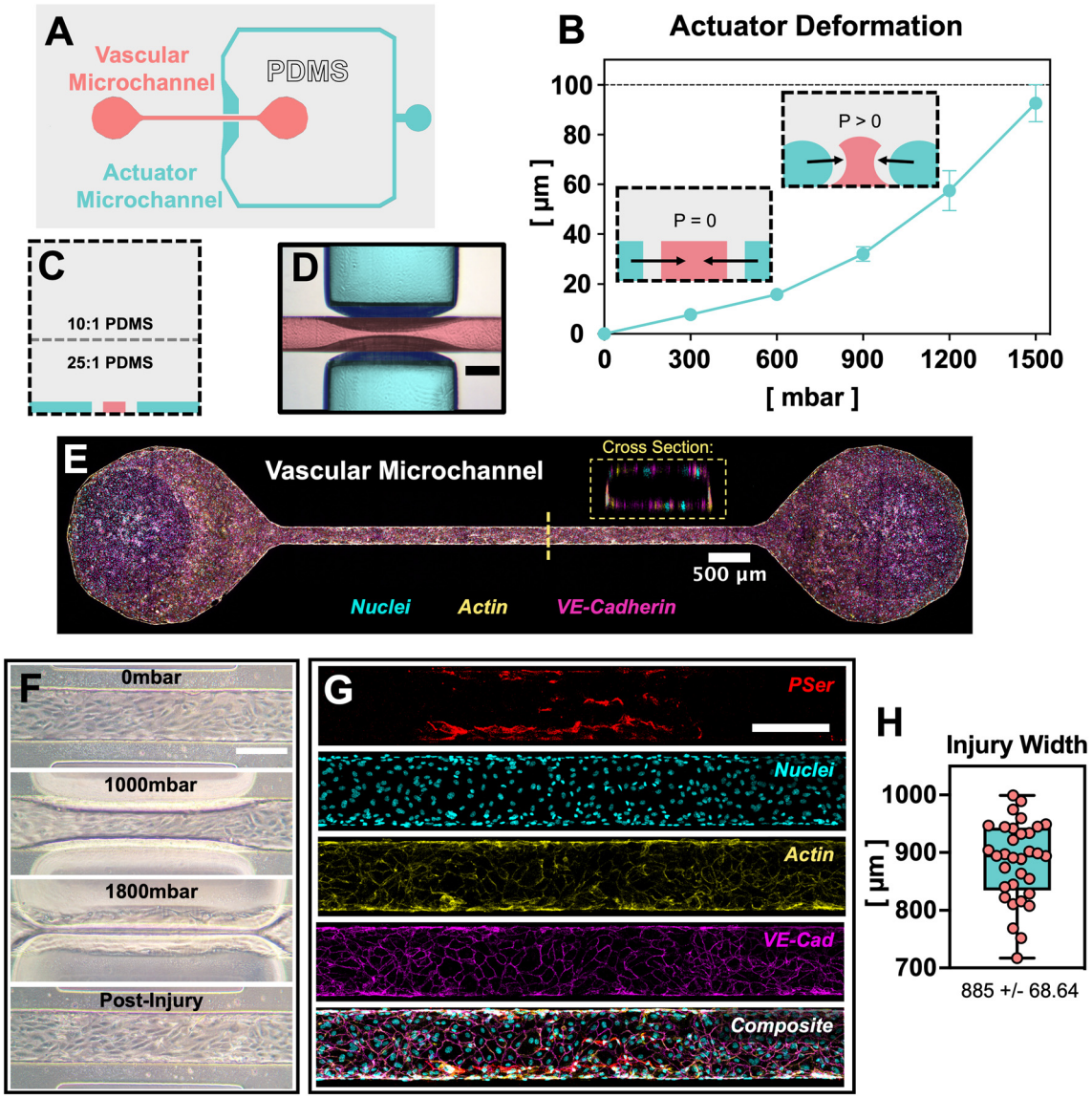

Fig. 1 A microvascular pressure injury-on-a-chip: "PINCH." A) top-down schematic of microchannel design. A closed microchannel flanks a straight, vascular microchannel on two sides. B) When the actuator microchannel is pressurized, the PDMS walls between the actuator microchannel and vascular microchannel deform inward (mean ± SD, n = 6). For the 200 µm × 100 µm (w x h) vascular microchannel depicted here, actuator walls make initial contact at 1500 mbar. C) Deformation is enabled by curing a thin layer of soft, 25 : 1 PDMS immediately overtop microchannel molds. D) Deformation can be visualized *via* brightfield microscopy (scale: 200 µm). False colors are overlayed empty microchannels to indicate actuator and vascular microchannels. E) Confocal microscopy confirms staining for nuclei (cyan), F-actin (yellow) and VE-cadherin (magenta) *via* DAPI, phalloidin, and antibody staining, respectively. A patent lumen is confirmed by viewing the vascular microchannel cross section. F) Demonstration of HUVEC injury in a PINCH in phase contrast micrographs (scale: 200 µm). H) Confocal micrographs confirm antibody staining for the endothelial marker VE-cadherin (magenta) and annexin V staining for the cell death indicator phosphatidylserine (PSer, red). G) The width of injury regions is plotted as the apparent width of PSer-positive cells. Injury regions averaged 885 ± 68.64 µm (mean ± SD, n = 33).

devices were made of PDMS bonded to glass. A vascular microchannel was flanked on either side by an actuator microchannel, such that addition of pressure to the actuator microchannel compresses, or "pinches", the vascular microchannel (Fig. 1A–D). The 100 µm PDMS walls between each actuator microchannel segment and the vascular microchannel made initial contact when ~1500 mbar was applied to the actuator microchannel. For injury experiments, we applied 1800 mbar to ensure compression of the endothelium (Fig. 1F). Deformability was achieved by casting a soft, 25 : 1 w/w mix of PDMS elastomer and crosslinker mix overtop of the microchannel molds (Fig. 1C). The 10 : 1 w/w layer of PDMS poured on the pre-cured 25 : 1 made the PINCH devices easier to handle as the top surface was less adhesive. We applied pressure with an Elveflow Ob1 Mk3 pressure regulator (ESI† Video S1 and S2), but we also confirmed that closure pressure can be generated by manually compressing a column of air in a 10 mL syringe. To test the deformability of the actuator walls, we applied pressures between 0 and 1500 mbar. Return of applied

pressure to 0 mbar in the actuator channel returns the actuator wall segments to their original dimensions (Fig. 1F). The relationship between actuator microchannel pressure and actuator deformation can be approximated with a second order polynomial function (R^2 = 0.9788) (Fig. S1B†). Finally, we confirmed with confocal microscopy that a patent HUVEC endothelium is achieved in the vascular microchannels (Fig. 1E), wherein HUVEC successfully attach to all four cross sectional surfaces. HUVEC were successfully seeded as before, without the need to rotate microdevices to ensure attachment to all surfaces.[74]

3.2. Confirmation of injury and assessment of coagulation at injury sites

Presence of injury was confirmed with annexin V staining for phosphatidylserine exposure. Application of 1800 mbar of pressure to the actuator microchannel compressed the vascular microchannels and resulted in an average injury length of 885 ± 68.64 μm. Injury regions extended to a slightly greater width than the initial boundaries of the actuator microchannel (788 μm) due to expansion of the PDMS during actuator compression (Fig. 1F–H). Vascular injury in the PINCH devices was confirmed by staining PSer with annexin V-TRITC (Fig. 2B and C). PSer staining sufficiently identified injury regions after paraformaldehyde fixation (Fig. 1G) and during live cell imaging (Fig. 2A). Most PSer was identified on microchannel walls and ceilings, and cytosolic cell tracking dye is mostly visible after injury at the bottom of vascular microchannels (Fig. 2A). Perfusion of plasma spiked with fluorescently labeled fibrinogen revealed accumulation of fibrin at injury sites (Fig. 2A). Quantification of the fluorescent intensity of fibrin revealed that both pre-treatment with fluid shear stress and compression injury can alter coagulation levels (Fig. 2C). We observed the greatest average and the greatest variability in fluorescent fibrin accumulation in vascular microchannels that did not receive shear pre-treatment (2 826 037 ± 4 326 143 A.U. (arbitrary units)). A statistically significant difference ($p < 0.05$) was found in the fluorescent fibrin accumulation in injured vascular microchannels pre-treated with 5 dyne cm^{-2} (2 470 483 ± 1 326 696 A.U.) and both the injured (252 202 ± 54 263 A.U.) and uninjured (423 329 ± 181 758 A.U.) vascular microchannels pre-treated with 10 dyne cm^{-2} (Fig. 2C). Interestingly, less fibrin accumulation was detected in the injured vascular channels pre-treated with 10 dyne cm^{-2}

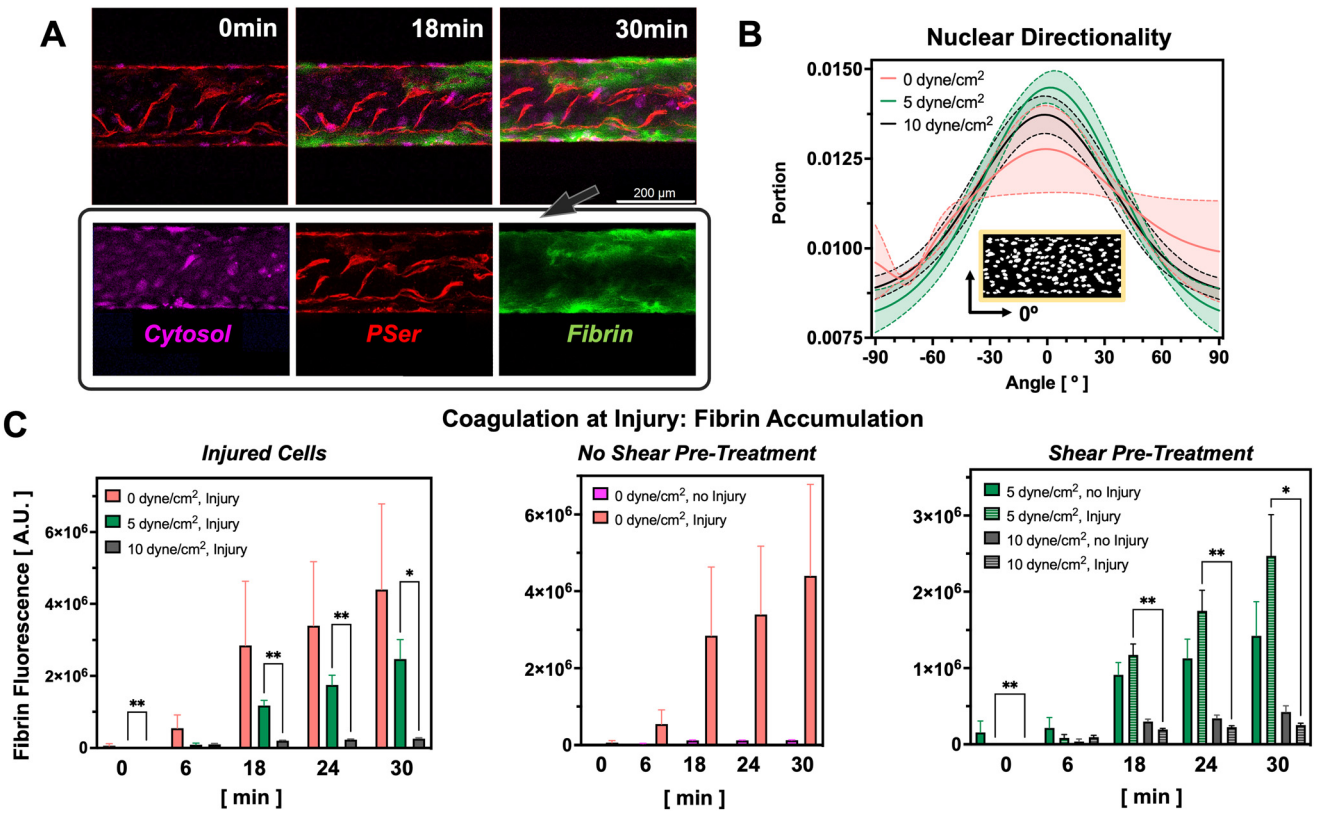

Fig. 2 Fluid shear stress and injury regulate coagulation levels in the PINCH devices. A) Confocal micrographs depicting accumulation of fluorescent fibrin (green) at PSer-positive (red) sites of vascular injury. Cytosolic dye (magenta) indicates uninjured cells. B) Nuclear directionality measurements reveal shear promotes more nuclear alignment along the direction of flow, 0° (n = 5). C) Pre-treatment of endothelium with fluid shear stress prior to injury limits subsequent coagulation (0 dyne cm^{-2} injury: N = 13; 0 dyne cm^{-2} no injury: N = 5; 5 dyne cm^{-2} injury: N = 6, 5 dyne cm^{-2} no injury: N = 5, 10 dyne cm^{-2} injury: N = 5, 10 dyne cm^{-2} no injury: N = 5; mean ± SEM, *$p < 0.05$, **$p < 0.01$, mixed-effects analysis). Greater coagulation levels are seen in injured vascular microchannels pre-treated with 0 and 5 dyne cm^{-2} shear stress as compared to 10 dyne cm^{-2}.

compared to the uninjured channels pre-treated with 10 dyne cm^{-2}. In injured vascular microchannels, coagulation levels trended downward with increasing magnitude of fluid shear stress pre-treatment (Fig. 2C). Fluid shear stress of 5 and 10 dyne cm^{-2} promoted greater HUVEC nuclear alignment along the direction of flow compared to maintenance in static conditions.

3.3. Evaluation of coagulation as an injury site response in the PINCH

Because recalcification of citrated plasma induces coagulation (Fig. S2†), we tested the extent to which injury promoted coagulation by measuring fibrin accumulation upstream of, at, and downstream of the injury site (Fig. 3 and S4†). A schematic of this quantification is provided in Fig. S4† for clarity. Fluorescent intensity patterns suggest injury does in fact enhance coagulation in the PINCH (Fig. 3B). Shear-pretreated and injured vascular microchannels were found to have an increase in fibrin fluorescence traveling from upstream to injury site. Fig. S3† provides a clear depiction of upstream thrombus formation in a vascular microchannel prepared without shear pre-treatment. Fluorescent intensity plot profiles along the length of a vascular microchannel suggest the lack of anticoagulant stimulus with static pre-treatment. PCC was calculated for fibrin and phosphatidylserine fluorescent signals. We found that in injured vascular microchannels that did or did not receive shear pre-treatment, the percent change in the PCC was greater in the 5 dyne cm^{-2} shear pre-treated vascular microchannels (214 ± 128.5%) than in the un-treated vascular microchannels (−76.83 ± 59.12%). Recalcification of citrated plasma does induce coagulation (Fig. 5 and S2†), but the compression injury of the HUVEC endothelium accelerates coagulation (Fig. 2 and 3). Injured vascular microchannels also demonstrated a small increase in downstream fibrin fluorescence relative to upstream sites (Fig. 3 and S6†). Overall, however, the increase was most pronounced at injury sites. Injury locations contain damaged cell matter, but also provide exposure to underlying ECM, providing plasma with coagulation triggers as well as fibrin–ECM interaction sites, whereas fibrin accumulation in downstream locations is primarily dependent upon upstream activation. Unlike fibrin, no variation in vWF was detected along the length of the vascular channel (Fig. S6†). The mean fluorescent intensity of vWF was higher in 10 dyne cm^{-2} shear pre-treated vascular microchannels (176.2 ± 20.3 A.U.) compared to 5 dyne cm^{-2} (53.5 ± 32.8 A.U.) (Fig. S6†).

3.4. Evaluation of aberrant coagulation in the PINCH with hemophilic plasma

Once we confirmed that PINCH devices enable coagulation as an injury response, we compared the coagulation response of normal plasma to hemophilic plasma. The overall fluorescent intensity of hemophilic plasma fibrin (500 455 ± 106 399 A.U.) was dramatically lower than in normal plasma (2 470 483 ± 1 326 696 A.U.), reaching

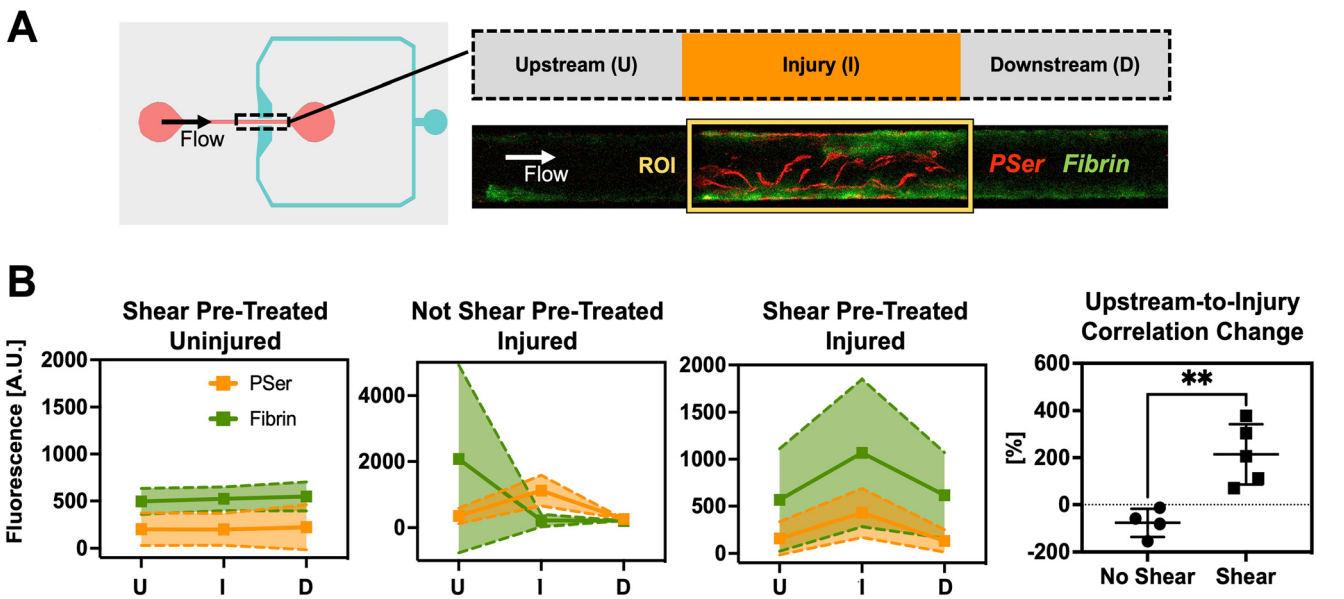

Fig. 3 Pre-treatment with extended fluid shear encourages injury site-specific coagulation during plasma perfusion. A) Fluorescent intensity of fibrin and phosphatidylserine was measured at, upstream, and downstream of injury sites. ROI were 900 μm wide and 240 μm tall. B) Fibrin intensity trends indicate that endothelium pre-treated with 5 dyne cm^{-2} fluidic shear stress are more efficient at capturing coagulation as an injury response compared to endothelium maintained at 0 dyne cm^{-2}. Endothelium not pre-treated with fluidic shear stress are more likely to allow clotting upstream of injury sites. Pearson's correlation coefficient was calculated for fibrin and PSer. The percent change in PCC from upstream-to-injury depicts coagulation as being amplified by the injury. Correlation changes were compared with an unpaired, two-tailed Student's *t*-test $^{**}p = 0.0043$. (Mean ± SD, $n = 4$–5).

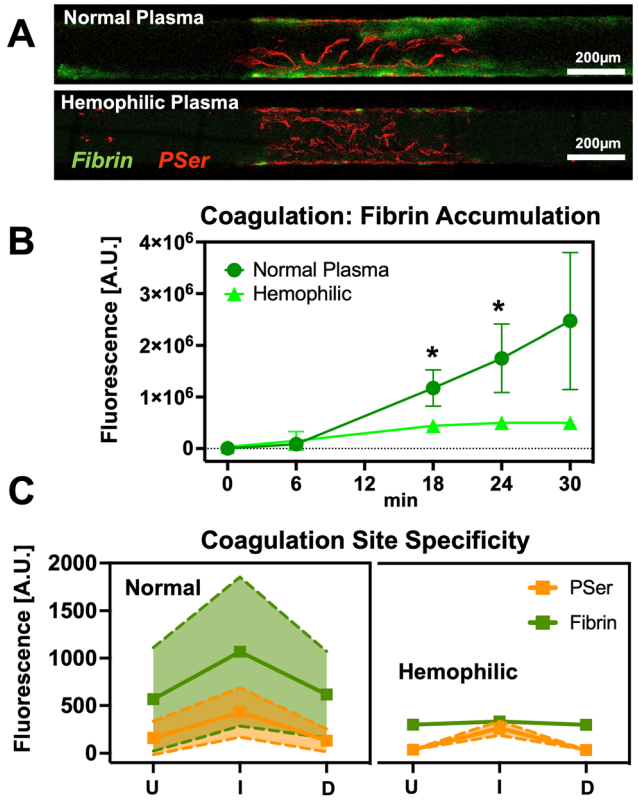

Fig. 4 Demonstration of reduced coagulation in hemophilic plasma. A) Confocal micrographs of vascular microchannel segments depict reduced coagulation of hemophilic plasma relative to controls. Although coagulation is reduced in hemophilic samples, an injury response is still visible as small regions of fibrin accumulation at the PSer-positive injury site. B and C) Quantification of fluorescent fibrin intensity reveal the coagulation response to injury is muted in hemophilic plasma. (Mean ± SD, n = 4–5, *$p < 0.05$, 2-way ANOVA).

significant difference ($p < 0.05$, two-way ANOVA) at 18 and 24 min of perfusion (Fig. 4B). Despite the reduced levels of coagulation in hemophilic plasma, PINCH devices were still able to capture an injury response of hemophilic plasma, confirming an increase in the fluorescent intensity levels of fibrin from upstream to injury site (Fig. S7†).

3.5. Demonstration of the PINCH for therapeutic screening

Thus far, MPS have primarily been leveraged for evaluation of drug toxicological safety, however, MPS are also interesting for evaluation of therapeutic performance.[55,75] To that end, we used the PINCH devices to test two formulations of therapeutic particles that have been recently demonstrated to enhance hemostasis or disrupt coagulation with a fibrinolytic agent.[61,65] Coagulation tests in the PINCH devices confirmed the expected behavior of each particle. The hemostatic Frag-E PLPs enhanced the average level of fluorescent fibrin accumulation at injury sites (592 867 ± 323 044 A.U.), while the fibrinolytic tPA-FSNs lowered the average level of fibrin accumulation (237 873 ± 26 391 A.U.), compared to controls (426 782 ± 81 248 A.U.) (Fig. 5A). Confocal images of statically prepared plasma clots corroborate the trends seen in the PINCH devices (Fig. 5B). The relative number of image pixels occupied by fibrin fibers and background indicates the density of fibrin is increased by Frag-E PLPs (1.333 ± 0.1308) and decreased by tPA-FSNs (0.3819 ± 0.1208) relative to controls clots (0.8504 ± 0.2654).

4. Discussion

Here we have reported PINCH, an on-chip device for pressure injury of a vascular endothelium. Injury is achieved in PINCH devices by pressurizing an actuator microchannel to induce lateral deformation of PDMS walls to compress a vascular endothelium within a central microchannel (Fig. 1). The compression by lateral micro-actuation was achieved by curing an extra soft (25 : 1 base-to-crosslinker ratio) layer of PDMS immediately overtop of 3D printed molds (Fig. 1C). An additional layer of 10 : 1 PDMS was poured on top, so the layers of PDMS did not require additional alignment or plasma bonding steps. The compressive microactuator in the PINCH was inspired by a design previously used to sort *C. elegans* worms and peptides.[59,60] We miniaturized the dimensions to facilitate compression of a 200 μm wide 100 μm tall endothelialized microchannel. We found that full compression of the microchannel disrupts the endothelium (Fig. 1F–G and 2A). During normal coagulation, damage to the vascular endothelium reveals underlying basement membrane extracellular matrix (ECM) and releases tissue factor, which initiate the intrinsic and extrinsic coagulation pathways, respectively.[1–4,76,77] In the ~900 μm wide region of compression, cells are partially removed, but some cell debris remains, as confirmed by annexin V staining for phosphatidylserine (PSer). After injury, blood plasma may be perfused to assess coagulation at the site of vascular injury (Fig. 2A and C). As previously indicated, PSer is a convenient marker for endothelial cell damage, and an interesting marker for monitoring coagulation.[30] Though PSer is not thought to be strictly necessary for fibrin polymerization to occur, PSer is thought to accelerate coagulation by facilitating association of the coagulation factor complexes tenase and prothrombinase.[78] Although the Pearson's correlation coefficients (PCC) calculated for fibrin and PSer were low, ranging from −0.052 to 0.409, the percent change in PCC values from upstream to injury site was significantly higher in shear pre-treated (215%) vascular microchannels than untreated microchannels (−76.83%) (Fig. 3). These data clearly suggest that vascular damage helps to upregulate coagulation in recalcified plasma and corroborate findings that PSer plays a minor but positive role in promoting coagulation.[30]

To investigate the role that exposure of vascular endothelial cells to fluid shear stress plays in coagulation, we perfused vascular microchannels overnight at approximately 0, 5, or 10 dyne cm^{-2} with culture medium prior to injury. Continuous fluid shear is known to stimulate anticoagulant behavior of the vascular endothelium.[1,2,76,79] Normal levels of fluid shear disrupt platelet binding and activation by

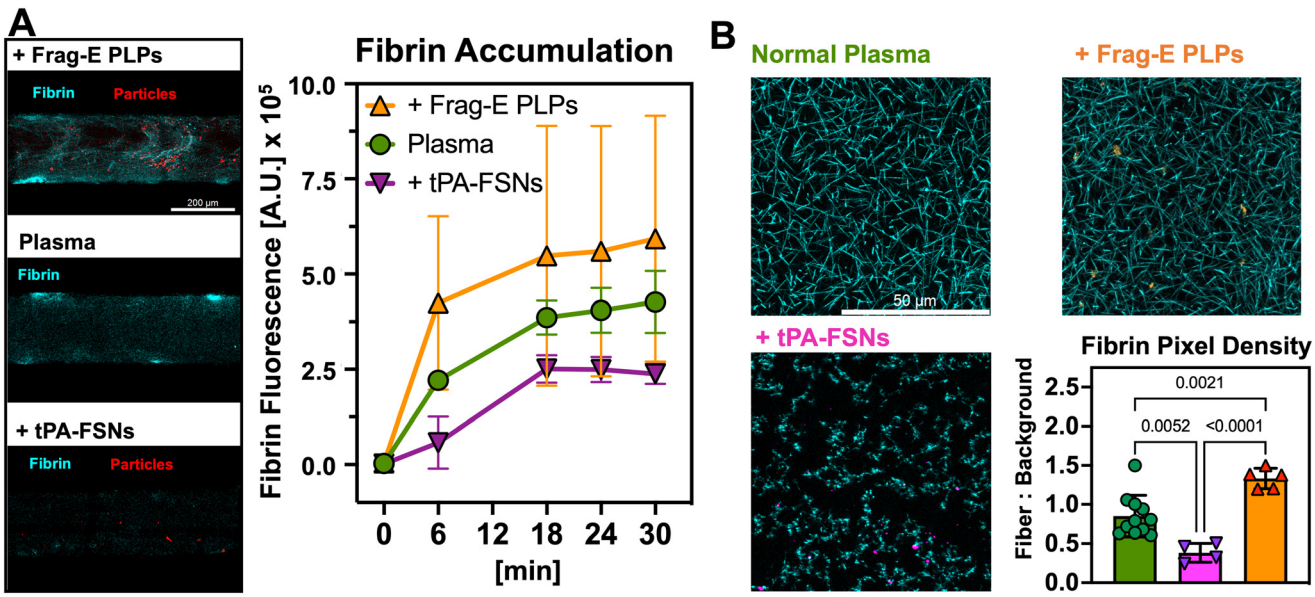

Fig. 5 Modification of coagulation with fibrin-binding microgels and nanogels. A) In the PINCH devices, coagulation levels of plasma supplemented with synthetic platelets confirm expected trends: Frag-E PLPs (n = 7) participate in coagulation by binding fibrin and collapsing *via* Brownian motion; tPA-FSNs (n = 3) disrupt coagulation by binding fibrin and releasing fibrinolytic tPA, halting the increase in coagulation seen in normal plasma (n = 4). (Mean ± SD). B) Confocal z-stack projections prepared on plain microscope slides confirm the trends seen in vascular microfluidics. The overall density of fibrin networks is increased or decreased by Frag-E PLPs and tPA-FSNs, respectively (mean ± SD, n = at least 3 slides, 1–3 images per slide; p-values displayed, one-way ANOVA).

promoting the release of nitric oxide and prostaglandin I_2 from vascular endothelial cells.[1,76] Fluid shear directly inhibits the coagulation cascade by promoting the endothelial cell expression of tissue factor pathway inhibitor, thrombomodulin, and endothelial protein C receptor. These proteins limit fibrin polymerization by binding to otherwise active coagulation factors. Accordingly, we found that static culture devices elicited both the greatest average and variability in coagulation level (Fig. 2C). By pre-treating vascular endothelium with fluid shear stress prior to injury and blood plasma perfusion, we observed a more pronounced injury-specific coagulation response. These findings corroborate results from a previous microvascular device,[69] which demonstrated an attenuation of platelet attachment to underlying collagen when a microvessel was pre-treated with fluid shear stress. Previous work has also demonstrated that shear stress improves HUVEC attachment to underlying matrix protein in microfluidic channels.[80] Altogether, perfusion of endothelial microchannels helps to improve endothelial integrity and limit blood cell and plasma protein interaction with underlying ECM. The attenuation of coagulation levels by pre-treating endothelium with fluid shear stress identifies an important consideration in MPS research, which is the emergence of tissue-level function when proper mechanical stimulus is provided.[49–51,81,82] Additional coagulation experiments, with hemophilic plasma and for therapeutic screening, were conducted after pre-treatment at 5 dyne cm^{-2} shear stress.

Unlike fibrin, vWF displayed no increase at injury sites in shear pre-treated, injured vascular microchannels. Previous research has shown that low levels of fluid shear stress are sufficient to induce vWF assembly on vascular endothelium, but higher levels of stress are necessary to induce assembly on ECM.[83] While we did detect a higher overall production of vWF in vascular channels pre-treated at 10 dyne cm^{-2} compared to 5 dyne cm^{-2}, our results suggest this dictated by endothelial response to pre-injury treatment conditions, and not plasma perfusion. The shear response in vWF production supports previous work showing shear stress stimulates greater vWF production in HUVEC.[84]

Perfusion of injured HUVEC in vascular microchannels with type A hemophilic plasma captured the limited coagulation response of hemophiliacs. In type A hemophilia, patients are deficient in coagulation factor VIII (FVIII). FVIII participates in a positive feedback loop of thrombin activation. By interrupting this loop, thrombin activation and fibrin polymerization happens much slower, and thicker fibrin fibers accumulate in less dense networks that are poor at stopping bleeding.[85–87] The PINCH devices conveniently captures an overall reduced coagulation of hemophilic plasma without the assembly of multiple layers of microfluidic housing. Coagulation levels of hemophilic plasma were significantly lower than in normal plasma (Fig. 4). Interestingly, hemophilic plasma still displayed an injury response, in that a greater amount of fibrin accumulated at injury sites relative to upstream of the injury (Fig. 4 and S7†). This spike in even hemophilic plasma is a promising indication of the ability of the PINCH devices to capture coagulation as an injury specific response.

Previously, our laboratory has developed a synthetic platelet technology that mimics the fibrin-binding and contractile properties of platelets.[62] Ultra-low crosslinking density of pNIPAm microgels, coupled to fibrin-binding motifs, allows the platelet-like particles (PLPs) to promote clotting *in vitro* and *in vivo*. Our lab has engineered various formulations of these particles to further optimize their performance. Our lab has also explored fibrin-targeted nanogel designs for targeted delivery of fibrinolytics. This tPA-FSN is a core–shell nanogel that achieves fibrin-binding as well as release of the fibrinolytic agent tPA. While these PLPs and tPA-FSNs have recently shown promising safety and efficacy in rodent and porcine models,[61,63] we understand that MPS offers a promising complement to animal models and a bridge to future human studies, because MPS allow us to capture human physiology with human cells.[5,50,55] Assessment of Frag-E PLPs and tPA-FSNs with the PINCH devices demonstrated promising confirmation of expected behavior: Frag-E PLPs participate in coagulation and enhance fibrin density, while tPA-FSNs disrupt coagulation and limit fibrin accumulation (Fig. 5). These demonstrations make the PINCH devices a promising candidate for additional therapeutic screening. Because the PINCH devices can capture fibrin accumulation as a vascular injury response, it could help inform future modifications of PLPs, such as change in accumulation rate of PLPs outfitted with collagen or fibronectin-specific binding motifs.

A limitation of our study is the time between shear pre-treatment, injury, and coagulation. These steps were carried out sequentially, with time taken to dye phosphatidylserine and transport devices to a room for confocal imaging. Time in between removal from pumps and plasma perfusion during confocal imaging totaled approximately 25 min. These interruptions are commonplace in microfluidics experiments but might artificially promote a pro-coagulant phenotype in the vascular endothelium due to the disruption of shear stimulus. Future studies would benefit from attempts to perfuse blood in microvessels for hours to days, in place of culture media perfusion. Such tests would inform the limitations of anticoagulants, including robustness of the microvessels themselves. The exact mechanism(s) that support coagulation in platelet-depleted plasma in devices such as the PINCH is not definitive. Many studies proceed with the experimental use of vascularized MPS after hours or days of perfusion shear stress,[29,30,66,69,88] and extended exposures to shear stress have been shown to increase endothelial barrier integrity for weeks.[89] Accordingly, extended pre-treatment of the PINCH devices with perfusion shear stressed could significantly impact the anticoagulant properties of the endothelium. This effect is of particular interest for future studies, when perfusing whole blood, as extended preconditioning may reduce platelet adhesion by promoting tighter endothelial cell–cell junctions. Furthermore, the application of increasing actuator channel pressure over time may also permit investigation of dynamic stenosis, which modulated shear stress, on resident endothelial cells.

PINCH devices were prepared with pooled HUVEC to limit donor variability, but a future promise of MPS is to improve analytical throughput and patient-specific evaluation of physiology and drug response.[49,50,75] While HUVEC are popular for demonstration of MPS funcitons,[18,29–32,42,66,80,90,91] using alternative endothelial cell types, *e.g.*, dermal or brain microvascular cells, will be valuable for studying vascular and hemostatic responses in different tissues. Since skeletal muscles make up most of the body's mass and traumatic injury often involves damage to these tissues, these cell types are particularly relevant for understanding vascular responses in injury contexts. Additionally, specifications of endothelial cell type, such as venous, arterial, or lymphatic, would also warrant experimental matching of fluid shear stresses experienced by specific cell types *in vivo*, which is possible with the PINCH device.

It should also be noted that these studies only used immunofluorescence staining, which is a limitation of the current study. The availability of relatively low cell counts is an emerging challenge for expanded analyses of some MPS,[69] including the PINCH device. Larger or multiplexed PINCH designs, which house more cells, could more readily permit biochemical analyses. Future studies will include validation using further analytical techniques including mass spectrometry and molecular assays (*e.g.* ELISAs, and/or qPCR).

Lastly, it is worth noting the limitation of MPS development with PDMS. It has long been established that PDMS suffers from adsorption and absorption of small and hydrophobic molecules.[92] If more rigid, less absorbent plastics replace PDMS for vascular microfluidic housing, it will be critical to consider alternative approaches to the induction of injury or mechanical stimulation in general, which is achieved with deformation of soft PDMS in devices like the PINCH. Ongoing research seeks to permit continued use of PDMS with chemical modifications of PDMS that reduce drug absorption.[92]

While MPS have captured both clot formation and degradation, no device has captured the automatic transition from clot formation to degradation.[93–100] Researchers have successfully formed and then degraded clots in microfluidics, but the transition was controlled with manual provision of exogenous pro-coagulant solutions, followed by fibrinolytic solutions. No system has facilitated the transition from coagulant to fibrinolytic states as regulated by cells and blood alone. A more complete recapitulation of clot progression will require extended perfusion time and the optimization of blood recalcification or CTI levels. Approximately 0.01 M of $CaCl_2$ is a popular concentration for recalcification, but it also facilitates complete polymerization of fibrinogen into fibrin in a citrated blood sample. Lower recalcification concentrations might allow extended maintenance of blood in its liquid phase without compromising inherent clottability. It would also be pertinent to investigate hemostasis *in vitro* in more highly branched networks. *In*

vivo, vasoconstriction can help divert blood flow to uninjured vessels within a parallel network, preventing complete thrombus in a particular region. For highly branched capillary networks, temporary thrombus of a region can be accommodated by the high density of the network, such that nearby vessels may assist in transport until an occluded vessel or wounded region reopen or anastomose with unobstructed vessels *via* angiogenesis. A single linear microfluidic channel would fail to capture this coordinated response. More highly branched vascular geometry may benefit hematological research as well as MPS research. Integration of multi-organ chip networks would also benefit from parallel assembly and branched vascular microchannels because organs are organized in parallel *in vivo* and greater branching *in vitro* would prevent thrombus in a particular location from obstructing an entire network of chips otherwise connected in series.

Research and development of vascular microfluidics adopted a challenge present in blood banking: the maintenance of blood in its liquid state for an extended time. Blood plasma contains numerous enzymatic triggers to initiate coagulation *via* the coagulation cascade. Although critical *in vivo*, coagulation in a closed microfluidic system can prevent extended use or perfusion of the microfluidic. Once blood is removed from the body, it loses its primary coagulation inhibitor, the vascular endothelium. It is the separation of blood from a robust vascular endothelium that triggers coagulation. Therefore, blood samples are usually mixed with anticoagulants such as corn trypsin inhibitor (CTI), heparin, sodium citrate, or ethylenediamine tetraacetic acid (EDTA). CTI inhibits coagulation factor XIIa, heparin activates antithrombin, and citrate and EDTA chelate calcium. Because anticoagulants have different mechanisms of action, we must understand the limitations of a particular anticoagulant and the method of anticoagulant during experimentation.[17] For example, the inhibition of factor XIIa by CTI silences the contribution of the intrinsic coagulation cascade to fibrin polymerization. For devices that seek to capture coagulation in its entirety, in which both the intrinsic and extrinsic pathways are activated, it is ideal to avoid the use of CTI. One microfluidics-based solution to the anticoagulant problem is on-chip recalcification.[17] Hydrodynamic mixing of citrated blood with a calcium solution allows blood recalcification immediately upstream of coagulation zones. Ideally, more microfluidic coagulation tests should leverage on-chip mixing, as well as integrate vascular and adventitial cells because cells that surround vasculature are known to coordinate the full hemostatic response, such as in tissue factor release or vasoconstriction. Recently, our group described a method for the fabrication of a microfluidic blood-tissue interface (BTI) that allows a blood vessel endothelium to contact a cell-embedded hydrogel without phase guides or synthetic membranes separating the endothelium and hydrogel.[74] Models like the BTI could be readily adapted to incorporate the actuators present in the PINCH devices, enabling analysis of coagulation in a multicellular system, whereby non-vascular cells could contribute to endothelial barrier integrity or production of tissue factor upon injury. Our actuator scheme could also be integrated into vascular models prepared by viscous finger patterning hydrogel lumen.[101,102] Finally, non-vascular cells could also be readily incorporated into the hemostasis model presented by Poventud-Fuentes *et al.* Such a toolbox of vascular injury models could allow researchers to compare hemostasis under conditions of crush and puncture injuries and evaluate differential treatment responses.

5. Conclusion

This work provides a new method to induce coagulation in a vascular microchannel. We found that lateral actuator compression is sufficient to damage a vascular endothelium and promote coagulation within a HUVEC endothelium. Pre-treating HUVEC endothelium with 0 or 5 dyne cm^{-2} revealed that shear stress promotes more selective coagulation at locations of HUVEC injury and reduces the tendency for non-specific coagulation upstream of injury sites. The performance of the PINCH devices was further demonstrated by confirming the diminished coagulation response of hemophilic plasma. Finally, we demonstrated the utility of the PINCH devices in drug screening by confirming expected behavior of hemostatic microgels and fibrinolytic nanogels. We believe these devices offer a valuable approach to studying the performance of therapeutics that target coagulation and offer insight into techniques for the analysis of coagulation or drug delivery in microphysiological systems. Future studies seek to integrate additional vascular and adventitial cells as well as whole blood perfusion to improve physiological mimicry of hemostasis.

Data availability

All data associated with this study are present in the paper or the ESI.† Raw data that support the findings of this study are available from the corresponding authors, M. D. and A. C. B., upon reasonable request.

Author contributions

H. D., A. B., and M. D. conceived the project. H. D. and E. B. conducted experiments and collected and analyzed data. S. P. and A. S. synthesized Frag-E PLPs and tPA-FSNs, respectively. H. D., S. P., A. S., A. B., and M. D. wrote and revised the paper.

Conflicts of interest

A. B. is a cofounder and stockholder of SelSym Biotech Inc. A. B. is an inventor on US Patent 10195304 and continuation in part 11419948B2 entitled "Functionalized microgels with fibrin binding elements", licensed by SelSym.

Acknowledgements

H. D. was supported by the Comparative Medicine Institute and a Pre-Doctoral Training Program at NC State University (NIH Grant T32-GM133393). A. S. was supported by NIH 1T32GM133366 and A. S. and S. P. were supported by NSF Graduate Research Fellowships. This research was supported by the National Science Foundation (CCSS-1846911, EBMS-2211404, and BMAT-1847488), the American Heart Association (22TPA969368), and the NC State Chancellor's Innovation Fund.

References

1 J. W. Yau, H. Teoh and S. Verma, *BMC Cardiovasc. Disord.*, 2015, **15**, 1–11.
2 T. C. Nguyen and J. A. Carcillo, in *Pediatric Clinical Care*, Springer, 2021, pp. 55–75.
3 P. Pradella, F. Tomasella and L. Mascaretti, in *Hemocoagulative Problems in the Critically Ill Patient*, Springer, 2012.
4 S. McRae, in *Mechanisms of Vascular Disease*, Springer, 2020, pp. 199–213.
5 R. Alonso-Roman, A. S. Mosig, M. T. Figge, K. Papenfort, C. Eggeling, F. H. Schacher, B. Hube and M. S. Gresnigt, *Nat. Microbiol.*, 2024, **9**, 891–904.
6 B. M. Trevisan, C. D. Porada, A. Atala and G. Almeida-Porada, *Semin. Cell Dev. Biol.*, 2021, **112**, 1–7.
7 T. V. Colace, G. W. Tormoen, O. J. McCarty and S. L. Diamond, *Annu. Rev. Biomed. Eng.*, 2013, **15**, 283–303.
8 S. Zhu, B. A. Herbig, R. Li, T. V. Colace, R. W. Muthard, K. B. Neeves and S. L. Diamond, *Biorheology*, 2015, **52**, 303–318.
9 P. H. Mangin, K. B. Neeves, W. A. Lam, J. Cosemans, N. Korin, S. W. Kerrigan, M. A. Panteleev and B. Subcommittee on, *J. Thromb. Haemostasis*, 2021, **19**, 582–587.
10 K. B. Neeves, A. A. Onasoga and A. R. Wufsus, *Curr. Opin. Hematol.*, 2013, **20**, 417–423.
11 D.-H. Ham, J.-S. Choi, J.-H. Choi and W.-T. Park, *Micro Nano Syst. Lett.*, 2023, **11**, 1–10.
12 H. Jigar Panchal, N. J. Kent, A. J. S. Knox and L. F. Harris, *Molecules*, 2020, **25**, 1–31.
13 J. Zilberman-Rudenko, J. L. Sylman, H. H. S. Lakshmanan, O. J. T. McCarty and J. Maddala, *Cell. Mol. Bioeng.*, 2017, **10**, 16–29.
14 R. Li, H. Elmongy, C. Sims and S. L. Diamond, *J. Trauma Acute Care Surg.*, 2016, **80**, 440–449.
15 A. Y. Mitrophanov, V. Govindarajan, S. Zhu, R. Z. Li, Y. C. Lu, S. L. Diamond and J. Reifman, *Biomech. Model. Mechanobiol.*, 2019, **18**, 1461–1474.
16 R. M. Schoeman, K. Rana, N. Danes, M. Lehmann, J. A. Di Paola, A. L. Fogelson, K. Leiderman and K. B. Neeves, *Cell. Mol. Bioeng.*, 2017, **10**, 3–15.
17 M. Lehmann, A. M. Wallbank, K. A. Dennis, A. R. Wufsus, K. M. Davis, K. Rana and K. B. Neeves, *Biomicrofluidics*, 2015, **9**, 064106.
18 P. F. Costa, H. J. Albers, J. E. A. Linssen, H. H. T. Middelkamp, L. van der Hout, R. Passier, A. van den Berg, J. Malda and A. D. van der Meer, *Lab Chip*, 2017, **17**, 2785–2792.
19 W. S. Nesbitt, E. Westein, F. J. Tovar-Lopez, E. Tolouei, A. Mitchell, J. Fu, J. Carberry, A. Fouras and S. P. Jackson, *Nat. Med.*, 2009, **15**, 665–673.
20 D. A. Kim and D. N. Ku, *Blood Adv.*, 2022, **6**, 2872–2883.
21 D. H. Ham, J. S. Choi, P. H. Jeong, J. H. Kim, H. B. F. Marcial, J. H. Choi and W. T. Park, *BioChip J.*, 2023, **17**, 478–486.
22 T. V. Colace and S. L. Diamond, *Arterioscler., Thromb., Vasc. Biol.*, 2013, **33**, 105–113.
23 X. Y. Hu, H. S. Chen, J. Li, K. L. Meng, Y. M. Wang and Y. J. Li, *Friction*, 2022, **10**, 128–141.
24 M. Li, D. N. Ku and C. R. Forest, *Lab Chip*, 2012, **12**, 1355–1362.
25 M. Li, N. A. Hotaling, D. N. Ku and C. R. Forest, *PLoS One*, 2014, **9**, e82493.
26 J.-S. Choi, D.-H. Ham, J.-H. Kim, H. B. F. Marcial, P.-H. Jeong, J.-H. Choi and W.-T. Park, *Micro Nano Syst. Lett.*, 2022, **10**, 1–7.
27 M. Lehmann, R. M. Schoeman, P. J. Krohl, A. M. Wallbank, J. R. Samaniuk, M. Jandrot-Perrus and K. B. Neeves, *Arterioscler., Thromb., Vasc. Biol.*, 2018, **38**, 1052–1062.
28 B. A. Herbig and S. L. Diamond, *Cell. Mol. Bioeng.*, 2017, **10**, 515–521.
29 I. Poventud-Fuentes, K. W. Kwon, J. Seo, M. Tomaiuolo, T. J. Stalker, L. F. Brass and D. Huh, *Small*, 2021, **17**, 1–12.
30 Y. Sakurai, E. T. Hardy, B. Ahn, R. Tran, M. E. Fay, J. C. Ciciliano, R. G. Mannino, D. R. Myers, Y. Z. Qiu, M. A. Carden, W. H. Baldwin, S. L. Meeks, G. E. Gilbert, S. M. Jobe and W. A. Lam, *Nat. Commun.*, 2018, **9**, 1–9.
31 L. Chen, Y. Zheng, Y. Liu, P. Tian, L. Yu, L. Bai, F. Zhou, Y. Yang, Y. Cheng, F. Wang, L. Zheng, F. Jiang and Y. Zhu, *Lab Chip*, 2022, **22**, 1344–1353.
32 E. T. Hardy, Y. Sakurai and W. A. Lam, *Methods Mol. Biol.*, 2022, **2373**, 159–175.
33 H. K. K. Yasuo Kubota, G. R. Martin and T. J. Lawley, *J. Cell Biol.*, 1988, **107**, 1589–1598.
34 M. Campisi, Y. Shin, T. Osaki, C. Hajal, V. Chiono and R. D. Kamm, *Biomaterials*, 2018, **180**, 117–129.
35 I. K. Zervantonakis, S. K. Hughes-Alford, J. L. Charest, J. S. Condeelis, F. B. Gertler and R. D. Kamm, *Proc. Natl. Acad. Sci. U. S. A.*, 2012, **109**, 13515–13520.
36 C. Hajal, G. S. Offeddu, Y. Shin, S. Zhang, O. Morozova, D. Hickman, C. G. Knutson and R. D. Kamm, *Nat. Protoc.*, 2022, **17**, 95–128.
37 S. G. Romeo, I. Secco, E. Schneider, C. M. Reumiller, C. X. C. Santos, A. Zoccarato, V. Musale, A. Pooni, X. Yin, K. Theofilatos, S. C. Trevelin, L. Zeng, G. E. Mann, V. Pathak, K. Harkin, A. W. Stitt, R. J. Medina, A. Margariti, M. Mayr, A. M. Shah, M. Giacca and A. Zampetaki, *Nat. Commun.*, 2023, **14**, 5552.
38 C. Weinberg and E. Bell, *Science*, 1986, **231**, 397–400.

39 K. A. DiVito, M. A. Daniele, S. A. Roberts, F. S. Ligler and A. A. Adams, *Data Brief*, 2017, **14**, 156–162.
40 K. A. DiVito, M. A. Daniele, S. A. Roberts, F. S. Ligler and A. A. Adams, *Biomaterials*, 2017, **138**, 142–152.
41 S. A. Roberts, K. A. DiVito, F. S. Ligler, A. A. Adams and M. A. Daniele, *Biomicrofluidics*, 2016, **10**, 1–12.
42 S. Sasaki, T. Suzuki, K. Morikawa, M. Matsusaki and K. Sato, *Micromachines*, 2023, **14**, 1–18.
43 S. H. Jung, B. H. Jang, S. Kwon, S. J. Park, T. E. Park and J. H. Kang, *Adv. Mater.*, 2023, **35**, 1–15.
44 Q. R. Jin, A. Bhatta, J. V. Pagaduan, X. Chen, H. West-Foyle, J. Y. Liu, A. Hou, D. Berkowitz, S. C. Kuo, F. B. Askin, T. D. Nguyen, D. H. Gracias and L. H. Romer, *Sci. Adv.*, 2020, **6**, 1–10.
45 C. G. Fonseca, V. Silverio, D. Barata, W. Giese, H. Gerhardt, S. Cardoso and C. A. Franco, *Microsyst. Nanoeng.*, 2023, **9**, 114.
46 M. T. Rogers, A. L. Gard, R. Gaibler, T. J. Mulhern, R. Strelnikov, H. Azizgolshani, B. P. Cain, B. C. Isenberg, N. J. Haroutunian, N. E. Raustad, P. M. Keegan, M. P. Lech, L. Tomlinson, J. T. Borenstein, J. L. Charest and C. Williams, *Sci. Rep.*, 2021, **11**, 12225.
47 A. Mehta, A. Desai, D. Rudd, G. Siddiqui, C. J. Nowell, Z. Tong, D. J. Creek, P. Tayalia, P. S. Gandhi and N. H. Voelcker, *Adv. Biol.*, 2022, **6**, e2200152.
48 S. R. Moses, J. J. Adorno, A. F. Palmer and J. W. Song, *Am. J. Physiol.*, 2021, **320**, C92–C105.
49 C. J. Mandrycky, C. C. Howard, S. G. Rayner, Y. J. Shin and Y. Zheng, *J. Mol. Cell. Cardiol.*, 2021, **159**, 1–13.
50 D. E. Ingber, *Nat. Rev. Genet.*, 2022, **23**, 467–491.
51 C. O'Connor, E. Brady, Y. Zheng, E. Moore and K. R. Stevens, *Nat. Rev. Mater.*, 2022, **7**, 702–716.
52 D. Ferrari, A. Sengupta, L. Heo, L. Pethö, J. Michler, T. Geiser, V. A. D. Perez, W. S. Zeinali, S. Zeinah and O. T. Guenat, *iScience*, 2023, **26**, 1–19.
53 Z. Chen, J. Lu, C. Zhang, I. Hsia, X. Yu, L. Marecki, E. Marecki, M. Asmani, S. Jain, S. Neelamegham and R. Zhao, *Nat. Commun.*, 2019, **10**, 2051.
54 P. Y. Chu, H. Y. Hsieh, P. S. Chung, P. W. Wang, M. C. Wu, Y. Q. Chen, J. C. Kuo and Y. J. Fan, *iScience*, 2023, **26**, 106927.
55 L. A. Low, C. Mummery, B. R. Berridge, C. P. Austin and D. A. Tagle, *Nat. Rev. Drug Discovery*, 2021, **20**, 345–361.
56 G. Shabestani Monfared, P. Ertl and M. Rothbauer, *Sci. Rep.*, 2020, **10**, 16192.
57 D. Sticker, S. Lechner, C. Jungreuthmayer, J. Zanghellini and P. Ertl, *Anal. Chem.*, 2017, **89**, 2326–2333.
58 G. Shabestani Monfared, P. Ertl and M. Rothbauer, *Pharmaceutics*, 2021, **13**, 1–14.
59 H. L. Adriana San-Miguel, in *WormBook: The Online Review of C. elegans Biology*, 2013, DOI: **10.1895/wormbook.1.162.1**.
60 S. Saberi-Bosari, M. Omary, A. Lavoie, R. Prodromou, K. Day, S. Menegatti and A. San-Miguel, *Sci. Rep.*, 2019, **9**, 7210.
61 E. P. Mihalko, K. Nellenbach, M. Krishnakumar, N. Moiseiwitsch, J. Sollinger, B. C. Cooley and A. C. Brown, *Bioeng. Transl. Med.*, 2022, **7**, e10277.
62 A. C. Brown, S. E. Stabenfeldt, B. Ahn, R. T. Hannan, K. S. Dhada, E. S. Herman, V. Stefanelli, N. Guzzetta, A. Alexeev, W. A. Lam, L. A. Lyon and T. H. Barker, *Nat. Mater.*, 2014, **13**, 1108–1114.
63 K. Nellenbach, E. P. Mihalko, S. Nandi, D. W. Koch, J. Shetty, L. Moretti, J. Sollinger, N. Moiseiwitsch, A. Sheridan, S. Pandit, M. Hoffman, L. V. Schnabel, A. Lyon, T. H. Barker and A. C. Brown, *Sci. Transl. Med.*, 2024, **16**, 1–13.
64 S. Nandi, K. Mohanty, K. Nellenbach, M. Erb, M. Muller and A. C. Brown, *ACS Biomater. Sci. Eng.*, 2020, **6**, 3026–3036.
65 A. Sheridan, K. Nellenbach, S. Pandit, E. Byrnes, G. Hardy, H. Lutz, N. Moiseiwitsch, G. Scull, E. Mihalko, J. H. Levy and A. C. Brown, *ACS Nano*, 2024, **18**, 15517–15528.
66 D. Nemcovsky Amar, M. Epshtein and N. Korin, *Micromachines*, 2019, **10**, 1–10.
67 J. Ahn, H. Lee, H. Kang, H. Choi, K. Son, J. Yu, J. Lee, J. Lim, D. Park, M. Cho and N. L. Jeon, *Appl. Sci.*, 2020, **10**, 1–14.
68 R. W. Muthard and S. L. Diamond, *Lab Chip*, 2013, **13**, 1883–1891.
69 W. J. Polacheck, M. L. Kutys, J. B. Tefft and C. S. Chen, *Nat. Protoc.*, 2019, **14**, 1425–1454.
70 S. N. Saw, C. Dawn, A. Biswas, C. N. Z. Mattar and C. H. Yap, *Biomech. Model. Mechanobiol.*, 2017, **16**, 197–211.
71 H. B. Musgrove, A. Saleheen, J. M. Zatorski, A. Arneja, C. J. Luckey and R. R. Pompano, *Micromachines*, 2023, **14**, 1–12.
72 S. Nandi, E. P. Sproul, K. Nellenbach, M. Erb, L. Gaffney, D. O. Freytes and A. C. Brown, *Biomater. Sci.*, 2019, **7**, 669–682.
73 E. P. Sproul, R. T. Hannan and A. C. Brown, in *Biomaterials for Tissue Engineering*, Humana Press, 2018, pp. 85–99, DOI: **10.1007/978-1-4939-7741-3_7**.
74 A. T. Young, H. Deal, G. Rusch, V. A. Pozdin, A. C. Brown and M. Daniele, *Organs-on-a-Chip*, 2023, **5**, 1–12.
75 J. Ko, D. Park, J. Lee, S. Jung, K. Baek, K. E. Sung, J. Lee and N. L. Jeon, *Nat. Rev. Bioeng.*, 2024, **2**, 453–469.
76 K. Neubauer and B. Zieger, *Cell Tissue Res.*, 2022, **387**, 391–398.
77 C. Aitken, V. Mehta, M. A. Schwartz and E. Tzima, *Nat. Cardiovasc. Res.*, 2023, **2**, 517–529.
78 H. M. Spronk, H. ten Cate and P. E. van der Meijden, *Thromb. Res.*, 2014, **133**(Suppl 1), S54–S56.
79 C. A. Dessalles, C. Leclech, A. Castagnino and A. I. Barakat, *Commun. Biol.*, 2021, **4**, 764.
80 T. Osaki, T. Kakegawa, T. Kageyama, J. Enomoto, T. Nittami and J. Fukuda, *PLoS One*, 2015, **10**, e0123735.
81 D. E. Ingber, *Biochem. J.*, 2023, **480**, 243–257.
82 H. E. Deal, A. C. Brown and M. A. Daniele, *J. Mater. Chem. B*, 2020, **8**, 7062–7075.
83 S. Gogia and S. Neelamegham, *Biorheology*, 2015, **52**, 319–335.
84 M. Galbusera, C. Zoja, R. Donadelli, S. Paris, M. Morigi, A. Benigni, M. Figliuzzi, G. Remuzzi and A. Remuzzi, *Blood*, 1997, **90**, 1558–1564.

85 L. D. Gray, M. A. Hussey, B. M. Larson, K. R. Machlus, R. A. Campbell, G. Koch, M. Ezban, U. Hedner and A. S. Wolberg, *Thromb. Res.*, 2011, **128**, 570–576.
86 R. Prodromou, B. Moore, W. Chu, H. Deal, A. S. Miguel, A. C. Brown, M. A. Daniele, V. Pozdin and S. Menegatti, *Adv. Funct. Mater.*, 2023, **33**, 1–13.
87 A. S. Wolberg, *Blood Rev.*, 2007, **21**, 131–142.
88 R. Barrile, A. D. van der Meer, H. Park, J. P. Fraser, D. Simic, F. Teng, D. Conegliano, J. Nguyen, A. Jain, M. Zhou, K. Karalis, D. E. Ingber, G. A. Hamilton and M. A. Otieno, *Clin. Pharmacol. Ther.*, 2018, **104**, 1240–1248.
89 L. Cucullo, P. O. Couraud, B. Weksler, I. A. Romero, M. Hossain, E. Rapp and D. Janigro, *J. Cereb. Blood Flow Metab.*, 2008, **28**, 312–328.
90 Y. Sun, B. Zhang and L. Xia, *Comput. Methods Programs Biomed.*, 2021, **208**, 106082.
91 N. Venugopal Menon, H. M. Tay, K. T. Pang, R. Dalan, S. C. Wong, X. Wang, K. H. H. Li and H. W. Hou, *APL Bioeng.*, 2018, **2**, 016103.
92 D. B. Mair, M. A. C. Williams, J. F. Chen, A. Goldstein, A. Wu, P. H. U. Lee, N. J. Sniadecki and D. H. Kim, *ACS Appl. Mater. Interfaces*, 2022, **14**, 38541–38549.
93 S. Loyau, B. Ho-Tin-Noe, M. C. Bourrienne, Y. Boulaftali and M. Jandrot-Perrus, *Arterioscler., Thromb., Vasc. Biol.*, 2018, **38**, 2626–2637.
94 D. Kim, S. M. Shea and D. N. Ku, *PLoS One*, 2021, **16**, e0247496.
95 C. S. Whyte, F. Swieringa, T. G. Mastenbroek, A. S. Lionikiene, M. D. Lance, P. E. van der Meijden, J. W. Heemskerk and N. J. Mutch, *Blood*, 2015, **125**, 2568–2578.
96 M. Sun, M. H. Hao Pontius, S. Yang, T. Pendekanti, S. Raghunathan, J. A. Shavit and A. Sen Gupta, *J. Thromb. Haemostasis*, 2023, **21**, 983–994.
97 L. M. Grobbelaar, C. Venter, M. Vlok, M. Ngoepe, G. J. Laubscher, P. J. Lourens, J. Steenkamp, D. B. Kell and E. Pretorius, *Biosci. Rep.*, 2021, **41**, 1–17.
98 R. Parente, M. R. Fumagalli, A. Di Claudio, C. L. Cardenas Rincon, M. Erreni, D. Zanini, G. Iapichino, A. Protti, C. Garlanda, R. Rusconi and A. Doni, *Pathogens*, 2023, **12**, 1–22.
99 H. Jiang, *Master of Science*, Boston University, 2019.
100 C. S. Whyte and N. J. Mutch, *Front. Cardiovasc. Med.*, 2022, **9**, 1054541.
101 L. L. Bischel, S. H. Lee and D. J. Beebe, *J. Lab. Autom.*, 2012, **17**, 96–103.
102 E. Delannoy, G. Tellier, J. Cholet, A. M. Leroy, A. Treizebre and F. Soncin, *Biomedicines*, 2022, **10**, 1–20.